Editors' Suggestion

Going Beyond the Causal Limit in Acoustic Absorption

Ho Yiu Mak,[1] Xiaonan Zhang,[1] Zhen Dong,[1] Susumu Miura,[2] Takuro Iwata,[2] and Ping Sheng[1,*]

[1]*Department of Physics, HKUST, Clear Water Bay, Kowloon, Hong Kong, China*

[2]*Research Division, Advanced Materials and Processing Laboratory, Nissan Motor Co., Ltd., 1, Natsushima-cho, Yokosuka-shi, Kanagawa 237-8523, Japan*

(Received 14 June 2021; revised 13 September 2021; accepted 30 September 2021; published 29 October 2021)

Dictated by the causality constraint, the existence of a minimum absorber thickness has set an almost insurmountable obstacle for the remediation of ultralow-frequency noise in the tens of Hz to 150 Hz regime, owing to the very large absorber thickness required. Here, we show that, by manipulating the boundary condition in a calculated manner on the backside of the absorber, the causal constraint can be circumvented, and broadband near-total absorption of ultralow-frequency acoustic waves may be realized with an absorber thickness that is an order of magnitude less than the causal minimum. Our work delineates a design paradigm for the ultralow-frequency acoustic absorbers.

DOI: 10.1103/PhysRevApplied.16.044062

I. INTRODUCTION

The causality principle states that the response of a material or structure at any given moment can depend only on what happened before that moment. When translated into mathematical language, this intuitive statement led to the well-known Kramer-Kronig relationship between the real and imaginary parts of the electromagnetic dielectric function, as well as an inequality relating the acoustic (or electromagnetic) absorption spectrum to a minimum sample thickness, $d_{\min}$. For airborne sound, the causal constraint dictates that the sample thickness, d, must satisfy the following relationship [1,2]:

$$d \geq \frac{1}{4\pi^2}\frac{B_{\text{eff}}}{B_0}\left|\int_0^\infty \ln[1-A(\lambda)]d\lambda\right| = d_{\min}, \qquad (1)$$

where $A(\lambda)$ denotes the absorption spectrum as a function of wavelength λ, B_0 is the atmospheric pressure (bulk modulus of air), and B_{eff} is the effective bulk modulus of the sample at the static limit. From Eq. (1), one can deduce that, if the sample thickness, d, is thin, then the high absorption of low-frequency sound would necessarily have either a very-narrow-frequency bandwidth, as experimentally verified [3], or a broader-frequency absorption spectrum but with a lower absorption level. In either case, this would mean that the remediation of real-world low-frequency noise, which is usually broadband in nature, could not possibly be accomplished except with a sample thickness that were comparable to or greater than a quarter of a wavelength or even larger. Hence, the causal minimum-thickness law is the basic reason why ultralow-frequency noise in the range of a few tens of Hz to 150 Hz constitutes one of the most pernicious sources of environmental pollution. Attempts have been made to absorb or block low-frequency sound energy by designed subwavelength metamaterials [1–28]. However, while these structures and resonators are successful in approaching the causality-constrained minimum thickness in the low-frequency regime, effective high absorption with a broad frequency band has still not been realized below 150 Hz with thin absorbers, a regime where the causal constraint requires the absorbers to be at least tens of centimeter thick to achieve near-total absorption over an extended frequency regime.

In this work, we show through both experiments and simulations that it is entirely possible to circumvent the causal limit on minimum absorber thickness, so that a near-total *broadband* absorption can be achieved in the range of 50 to 150 Hz with an absorber thickness of 2 cm or less, placed on a hard reflecting surface [29]. Such a thickness is many times thinner than the causal minimum evaluated with the relevant absorption spectrum. The excellent absorption performance is based on the effects associated with the long-overlooked consequences of the boundary condition on the backside of an absorber. In particular, we appeal to the acoustic soft-boundary condition (ASBC) that complements the usual acoustic hard-boundary condition (AHBC) for airborne sound. The latter is implicitly assumed as the sample backing, in the form of a displacement node, in the derivation of Eq. (1) for $d_{\min}$. Such super-ultralow-frequency absorbers, however, lose their advantages at higher frequencies, and therefore their applications can be regarded as complementary to those broadband metamaterial absorbers demonstrating excellent absorption performance starting at 350 Hz onward [1,2].

*sheng@ust.hk

In what follows, we detail the ASBC and its characteristics in Sec. II. We identify an *optimal* absorber thickness associated with the acoustic soft boundary in Sec. III. In Sec. IV, we show that the ASBC can be achieved with a hard-reflecting-surface backing with an open gap separating the sample and the hard wall. Subsequently, we describe in Sec. V the use of a *partial* ASBC, realized though sidewall openings, in not only lowering a hybrid-membrane resonator's resonance frequency, but also increasing its peak width. In particular, the partial ASBC can significantly relax the application requirements for open-space access, while maintaining the thin-sample-thickness advantage, thereby making such resonators particularly useful in absorbing ultralow-frequency noise when only confined spaces are available.

II. ACOUSTIC SOFT-BOUNDARY CONDITION

It is well known that the ASBC is an alternative boundary condition to the AHBC; the latter being the prevalent condition for airborne sound, as exemplified by the solid wall. The ideal ASBC can be characterized by a node in pressure modulation, p, so that its surface impedance is defined by $Z_{\mathrm{ASBC}} = p/u = i0^{-}$ [30–33], where u denotes the displacement velocity that is characterized by a boundary antinode, out of phase with p. The large u can create a high displacement-velocity zone at the backside of a porous absorber, leading to high absorption, resulting from the high relative-displacement velocity between air and the solid skeleton [5,34]. This effect is especially significant in the low-frequency regime, since the displacement velocity decays slowly away from the boundary. In contrast, an absorber placed on the AHBC cannot exhibit any significant absorption until its thickness exceeds one quarter of a wavelength. In Fig. 1(a), we show a photograph of our metallic mesh absorber used in this work, together with an enlarged view of the pores. Given their excellent thermal conductivity, our metallic mesh sample can effect an additional absorption mechanism of breaking the adiabaticity in sound propagation [4,5,35]. The use of metallic mesh at the end of an open impedance tube to reduce reflection is apparently not new and has been previously observed and analyzed [36,37].

The ASBC in the low-frequency regime can be realized experimentally by directly opening one end of the impedance tube, as illustrated schematically in the inset of Fig. 1(b). Due to scattering, the actual impedance of an open tube is given by [38–41]

$$\frac{Z_{\mathrm{open}}}{Z_0} = 0.25(kr)^2 - ik\delta_0, \tag{2}$$

where $r = 5$ cm is the radius of the impedance tube; k is the wave number; $Z_0 = \rho_0 c_0$ is the impedance of air; ρ_0 and c_0 are the density and sound speed of air, respectively; and $\delta_0 = 0.6133r$ is the analytically determined coefficient for the unflanged opening condition. The inset in Fig. 1(b) shows the measured real part of the reflection coefficient, Re[r] (red circles), with the open-tube condition, which demonstrates excellent agreement with the prediction obtained from Eq. (2) (blue solid line) and full-wave simulations carried out by COMSOL (green dashed line). Details of the full-wave COMSOL simulations are given in Appendix A. A slight discrepancy between the theoretical calculation and the full-waveform COMSOL simulation at higher frequencies can be attributed to the fact that, in the theoretical calculation using Eq. (2), a one-dimensional plane wave is assumed throughout, but, in the full-waveform simulations, the scattered waves are not necessarily in the theoretically assumed form.

From the inset of Fig. 1(b), it is clear that the ideal ASBC at the opening boundary (with a zero impedance value) can only be realized in the limit of vanishing frequency. At 50 Hz, Re[r] is found to be extremely close to -1, which suggests that the open boundary in this case can be treated as close to being an ideal ASBC. With increasing frequency, however, Re[r] is seen to deviate from -1, implying an increasing amount of scattered transmission through the opening. Hence, for the ASBC, there is a need to define a quantity, extinction (E), as

$$\begin{aligned}\text{extinction} = 1 - |\text{reflection}|^2 = \text{absorption} \\ + |\text{transmision}|^2.\end{aligned} \tag{3}$$

From Eq. (3), we note that, if extinction = absorption, then transmission must be zero.

Quantitatively, we can monitor the deviation of the ASBC from its ideal value by using Re[r]. Whenever Re[r] lies between -1 and 0, there can be some absorption-enhancement effect. When Re[r] crosses zero into the positive territory, the boundary condition shifts from being partially soft to partially hard.

In the main panel of Fig. 1(b), we compare the extinction performance of a 0.5-cm-thick sample, comprising 25 layers of the metallic mesh, placed in front of the tube's open end. In this case, an accurate measurement of absorption would need data on scattered transmission, requiring sensing sound amplitude in an anechoic chamber along a spherical surface surrounding the tube. Instead of such measurements, here, we use the full-waveform simulation with a large spherical boundary surrounding the impedance tube to obtain the absorption. Details of the simulation are given in Appendix B.

Acoustic impedance of a homogeneous isotropic material, Z_{eff}, can be characterized by its complex effective bulk modulus, κ_{eff}, and effective density, ρ_{eff}, so that $Z_{\mathrm{eff}} = \sqrt{\kappa_{\mathrm{eff}}\rho_{\mathrm{eff}}}$. The method used to extract κ_{eff} and ρ_{eff}, and their explicit values, can be found in Appendix A. From a sample's complex values of $\kappa_{\mathrm{eff}}(f)$ and $\rho_{\mathrm{eff}}(f)$ already

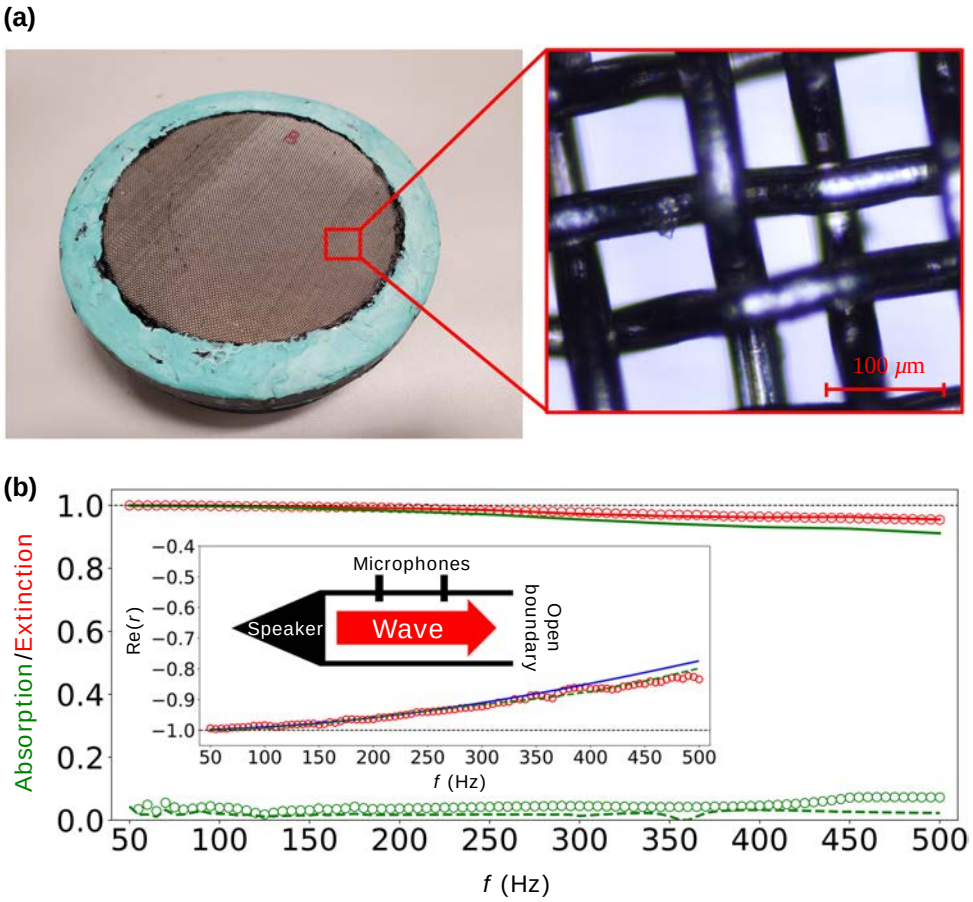

FIG. 1. (a) Photograph of the absorption sample (left panel) and an enlarged microscope image of the metallic mesh (right panel). Sample comprises layers of metallic meshes with an average pore size of 7.2×10^{-3} mm^2. (b) Inset, for the open boundary with no sample, we compare the real part of the reflection coefficient, Re[r], as a function of frequency obtained from experiments (red open circles), COMSOL simulation (green dashed line), and the prediction using the ASBC given by Eq. (2) (blue solid line). Excellent agreement is seen, especially below 300 Hz. Main figure shows the absorption and extinction for a 0.5-cm absorption sample placed in front of the open boundary, where red symbols and red solid lines represent the measured and simulated extinction, respectively, while the green solid line represents the simulated absorption. It is seen that the absorption and extinction results merge and become indistinguishable below 200 Hz, implying a negligible amount of scattered transmission in the low-frequency regime. Measured and simulated absorption results with the hard reflecting boundary are shown as green open circles and dashed line, respectively. Almost no absorption can be seen, as expected from the displacement-velocity nodal condition at the hard boundary.

obtained from the impedance tube's reflection and transmission measurements, we can predict the extinction, E, as a function of frequency by using the COMSOL full-wave simulation, as shown by the red line in Fig. 1(b). The simulated prediction is seen to agree very well with the measured results, as shown by the red open circles. By using the same material-parameter values, we obtain the simulated absorption, as shown by the solid green line. It is seen that the red line, red symbols, and the green line all merge below about 200 Hz. This is not surprising, since we expect almost total reflection at the opening surface below this frequency, so that the scattered transmission is negligible. If no reflection is detected, the energy must be dissipated. In the same main panel of Fig. 1(b), we show, as green open circles and a green dashed line, the absorption of the same 0.5-cm sample placed in front of a hard reflecting boundary. Almost no absorption can be seen for such a thin sample.

The absorption spectrum of the 0.5-cm sample, placed in front of a near-ideal ASBC, is extraordinary. If we compare this sample thickness with the minimum sample thickness predicted by Eq. (1) by using the absorption spectrum (green line) and taking $B_{\text{eff}} = B_0$, the calculated d_{min} is approximately 80 cm, which is 160 times larger than our sample thickness. We would like to emphasize that better absorption is expected for frequencies below 50 Hz, and hence, the advantage is even larger. The lower cutoff of 50 Hz is due to the measurement limitation of the impedance tube. However, rather than repudiating the causality constraint, which implicitly assumes a

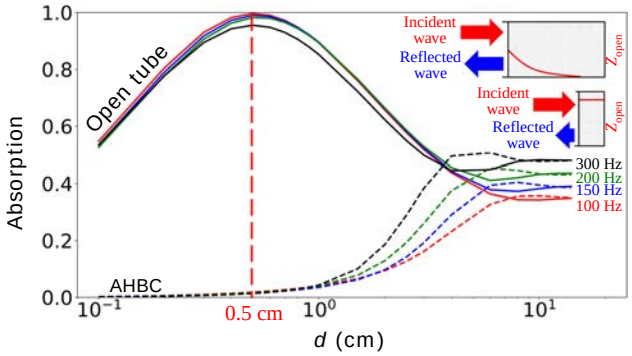

FIG. 2. Simulated absorption performance backed by ASBC (solid line) and AHBC (dashed line) at 100 Hz (red), 150 Hz (blue), 200 Hz (green), and 300 Hz (black), plotted as a function of sample thickness on the logarithmic scale. Two insets schematically illustrate the simulated displacement-velocity-amplitude distribution for a sound wave traveling inside an extremely thick (upper) absorber and a thin (lower) absorber, both backed by ASBC. Red lines indicate the wave amplitude inside the sample.

hard-boundary substrate, the purpose of this comparison is to show the huge advantage of *complementarity* offered by the ASBC in the ultralow-frequency regime, while the AHBC offers advantages at the higher frequencies.

III. OPTIMAL SAMPLE THICKNESS FOR THE ASBC

There is an optimal sample thickness for absorbers placed in front of an ASBC. Figure 2 illustrates the simulated absorption as a function of sample thickness d, plotted on a logarithmic scale, at different frequencies. Solid and dashed lines represent the absorption provided by samples with open and hard-boundary backing, respectively. The peaks of the solid lines indicate that the optimal thickness of the sample is around 0.5 cm, for frequencies between 100 and 300 Hz. Deviation from the optimal thickness would result in impedance mismatching, leading to worse absorption.

The peak in Fig. 2 is the result of two competing factors: accessibility to the ASBC at the backside of the sample and the absorption capability provided by the sample itself.

Consider a wave that travels through an extremely thick absorber with ASBC backing, as shown in the top inset of Fig. 2. The wave amplitude would decay exponentially to zero before it could reach the ASBC backing. This implies that the wave cannot access the absorption advantage offered by the ASBC. As a result, a thick absorber backed by either ASBC or AHBC would have the same absorption performance. It can be seen in Fig. 2 that the solid and dashed lines at the same frequencies join together as the sample thickness, d, increases beyond 10 cm. On the other hand, the lower inset in Fig. 2 shows another limiting case, where a wave travels through a very thin absorber. Although the wave can easily access the ASBC backing, the absorber is too thin to provide sufficient material to dissipate the incident wave. From the above discussion, it is clear that, starting from zero thickness, the absorption must increase, but when the sample is too thick the absorption will decrease as the thickness increases, because of the decreased accessibility to the absorption advantage offered by the ASBC. It follows that there must be an optimal in-between sample thickness for maximum absorption. While the existence of the optimal thickness is a general phenomenon for an absorber backed by the ASBC, the actual value of the optimal thickness can depend on the absorber material and structure. In our case, this optimal thickness occurs at about 0.5 cm for the metallic mesh with the given pore size.

An alternative view of the optimal sample thickness is that each layer of the metallic mesh will have a real part of the impedance, Z_r. The addition of N metallic layers, in series, will result in a total mesh impedance of $Z_{\text{eff}} = NZ_r$. In Eq. (A1) of Appendix A, we show that, when this Z_{eff}, in combination with the impedance on the backside of the sample, Z_b, can achieve impedance matching to Z_0, then total absorption can be attained with an optimal sample thickness.

IV. USING AN OPEN GAP AS THE SOFT BOUNDARY

Although the open-tube condition provides an excellent soft-boundary condition in the ultralow-frequency regime, it is impractical for actual applications, given that a hard-boundary backing is almost always present. We therefore propose to place the ASBC at 90° from the incident wave direction, i.e., by using an open gap, as illustrated by the inset of Fig. 3(a). In the same inset, we show Re[r] obtained from the simulation (green dashed line) and experiment (red circles) when an AHBC is placed 1.5 cm away from the tube opening. By using the same form of Eq. (2), the surface impedance of the gap opening on the side can be fitted by $Z_{\text{gap}}/Z_0 = 0.4(kr)^2 - ik(0.9)$. The best-fitted Re[$r$] from this form of Z_{gap} is plotted as the blue line in Fig. 3(a).

The gap ASBC induces an additional phase factor at the backside of the sample, which can affect the effective boundary condition, due to the additional travel distance, S (from the backside of the sample), needed to reach the gap opening on the side. To investigate this effect, we use the simple geometry shown in the inset of Fig. 3(b), where the backside of the sample is set at a distance, S, from the tube opening, for full-waveform simulations. We denote the additional phase at the backside of the sample the GP (geometric phase). We vary S and plot as solid lines the corresponding full-waveform-simulated Re[r] as a function of frequency in Fig. 3(b). Dashed lines in Fig.

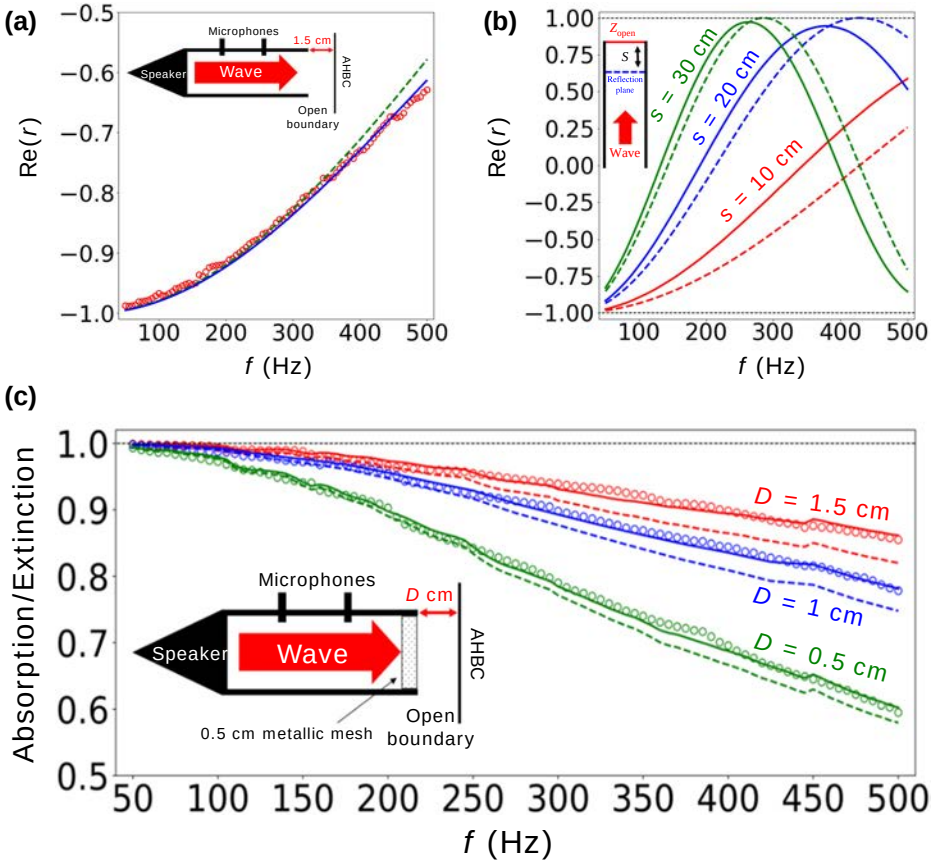

FIG. 3. (a) Placing a AHBC 1.5 cm away from the tube opening creates a "gap," as illustrated in the inset, which will shift the ASBC 90° from the incident wave direction. Re[r] obtained from experiment (red circles) and simulation (green dashed line) are shown. Blue line represents Re[r] obtained from the best-fitted gap impedance, $Z_{\text{gap}}/Z_0 = 0.4(kr)^2 - ik(0.9)$. (b) Simulated Re[$r$], using the configuration shown in the inset with $S = 10$, 20, and 30 cm, is plotted as a function of frequency, where S is the distance of the sample's backside to the opening. This illustrates the effect of the geometric phase (GP) on the ASBC. Dashed lines represent the calculated Re[r] with the GP given by $\cos[k(2S) + \pi]$. (c) Extinction results obtained from experiment (circles) and simulation (solid lines) plotted as a function of frequency for various gap sizes, D, as indicated. Corresponding absorption results obtained from simulation are plotted as dashed lines.

3(b) in different colors represent the corresponding Re[r] with the GP defined as $\cos[k(2S) + \pi]$, where π comes from the effect of the ASBC [30–33]. By comparing the solid and dashed lines with the same S, it is clear that the GP is the major factor that controls the frequency range exhibiting a negative Re[r]. In actual applications, the GP is mostly associated with the lateral size of the sample, i.e., by using a gap ASBC the lateral sample size should be small compared to the relevant wavelength range for good absorption.

We construct spacers through three-dimensional (3D) printing that can separate the absorber from the hard reflecting wall by a distance D. By placing the 0.5-cm-thick metallic mesh sample before the hard reflecting wall, as shown in the inset of Fig. 3(c), we measure the extinction with the gap sizes of $D = 0.5$ cm (green circles), $D = 1$ cm (blue circles), and $D = 1.5$ cm (red circles). The experimental results agree very well with the corresponding ones obtained from COMSOL simulations (solid lines with the same colors). The dashed lines denote the absorption provided by the same simulation. It is seen that, for the case of $D = 1.5$ cm, the absorption is over 96% below 200 Hz, and it is the dominant component of the extinction. Therefore, by including the 1.5-cm gap as part of the sample thickness, the total thickness of the sample would be 2 cm, which is approximately 36.5 times smaller than d_{min}, as suggested by Eq. (1).

The gap size, D, has a different effect from that of the GP (or S). From the symmetry of the wave-propagation path, it is clear that, at the middle of the circular cross section, there must be a "stagnation point," where the backside of the sample directly feels the reflection from the hard wall. Hence, in the neighborhood of the central region, the velocity antinode condition of the ASBC is mostly destroyed, and the absorption advantage is lost. When D decreases, such a "dead-zone" region increases in

size for any given frequency, until $D \to 0$ and the dead zone covers the whole backside of the sample. At that point, we have the AHBC. However, it should be noted that the effect of the gap size depends on the wave frequency. For low frequencies, such as close to 50 Hz, we can have a 0.5-cm gap size and the absorption can still reach about 99%. For higher frequencies, however, the gap size should be adjusted to be larger to attain good absorption.

So far, the ASBC is realized through the condition of an abrupt cross-section change in wave propagation, with the outside open space being very large as a precondition. However, in actual applications, such conditions may not always be available, as confined spaces are usually the scenario. Below, we show that, by employing a *partial* ASBC on the backside of the decorated-membrane resonators, the near-zero impedance condition can be greatly relaxed, so that no abrupt cross-section change or large outer space is required. The resulting absorption peak is not only in the ultralow-frequency range, but also has a much broader width than that with the AHBC hybrid resonance. Such absorbers have the promise of broad applications in the ultralow-frequency regime.

V. HYBRID-MEMBRANE RESONATOR WITH THE PARTIAL ASBC

We now demonstrate that, by manipulating the backside boundary condition of a decorated-membrane (DM) resonator in the hybrid geometry, i.e., backed by a shallow cavity, the absorption of broadband ultralow-frequency acoustic waves (<100 Hz) can be achieved with a sample thickness that is an order of magnitude below $d_{\min}$, as given by Eq. (1).

In earlier works [6,7,42,43], it was shown that, in a hybrid structure, comprising a decorated membrane set on a closed cavity of depth d, the required impedance of the membrane that can lead to zero reflection (and total absorption) is given by

$$Z_{\mathrm{DM}} = Z_0(1 - i \cot kd). \tag{4a}$$

Here, the bottom of the closed cavity is a hard reflecting wall that gives rise to a series impedance of $+iZ_0 \cot kd$ at the backside of the DM, leading to a total impedance, as perceived by the incoming wave, given by $Z = Z_{\mathrm{DM}} + iZ_0 \cot kd = Z_0$. It turns out that the condition set by Eq. (4a) for the decorated membrane can be satisfied in the lower side of the antiresonance frequency, leading to a narrow total-absorption peak [6]. If now we replace the hard-boundary condition at the bottom of the cavity by the soft boundary, then the condition for total absorption, Eq. (4a), becomes

$$Z_{\mathrm{DM}} = Z_0(1 + i \tan kd). \tag{4b}$$

From Eqs. (4a) and (4b), it follows that, for total absorption with the partial ASBC, the imaginary part of the membrane impedance can be interpolated between negative and positive infinity, depending on the phase factor, kd. This is reasonable, since the imaginary part of the impedance is (dominantly) the inverse of the real part of the Green function [6,7,42,43]. Close to a resonance frequency Ω, the inverse of the Green function is simply proportional to $\Omega^2 - \omega^2$. This means for the partially ASBC, like a DM backed by a cavity with sidewall holes, one can have the impedance-matching condition for the DM at a frequency lower than Ω, with a positive imaginary part, in contrast to the case of the hybrid resonance (with the AHBC), where the impedance matching has to occur at $\omega > \Omega$. To verify this, the required complex impedance-matching condition on a decorated membrane, when it is backed by a cavity with three sidewall openings, is plotted in Fig. 4(a) (solid lines) together with the normalized impedance for a decorated-membrane resonator (open circles) alone, obtained from measured data. The required impedance-matching condition is reached at the intersection between the solid blue line and the open blue circles, as designated by the red arrow in Fig. 4(a), which is far below the membrane's first eigenmode (black arrow) and the antiresonance frequency (black dashed arrow). Details of the impedance derivation (for the solid lines) can be found in Appendix C. Moreover, it is seen that the approximate matching of the real part of the impedance can be extended to a rather broad frequency range.

In the inset of Fig. 4(b), we show the measured (red circles) and simulated (red solid line) extinction data by a decorated membrane set on a 0.8-cm-deep cavity with three cylindrical sidewall openings (separated from each other by 120°) that are 0.5 cm in diameter and 1 cm in depth. The green squares in the same figure represent the simulated absorption, which almost completely overlaps with the extinction curve, thereby, from Eq. (3), it should be clear that the transmission component is negligible. Details of the simulation can be found in Appendix B. The inset shows a schematic illustration of the hybrid structure, together with a photograph of the sample. It is seen that the absorption can reach 99% at 81 Hz, with a full width at half maximum about 20–25 Hz. From the simulation results, this high absorption can be attributed to the dissipation arising from both the large vibration amplitude of the membrane and the high airflow velocity inside the holes. A figure showing the explicit airflow velocity and membrane-displacement field can be found in Appendix C. Such a broad near-total resonant absorption peak at ultralow frequency has not been usually observed for such a thin sample. Indeed, if we substitute the measured absorption spectrum into Eq. (1), we obtain $d_{\min} = 10.2$ cm, which is more than 12.5 times larger than the actual sample thickness of 0.8 cm.

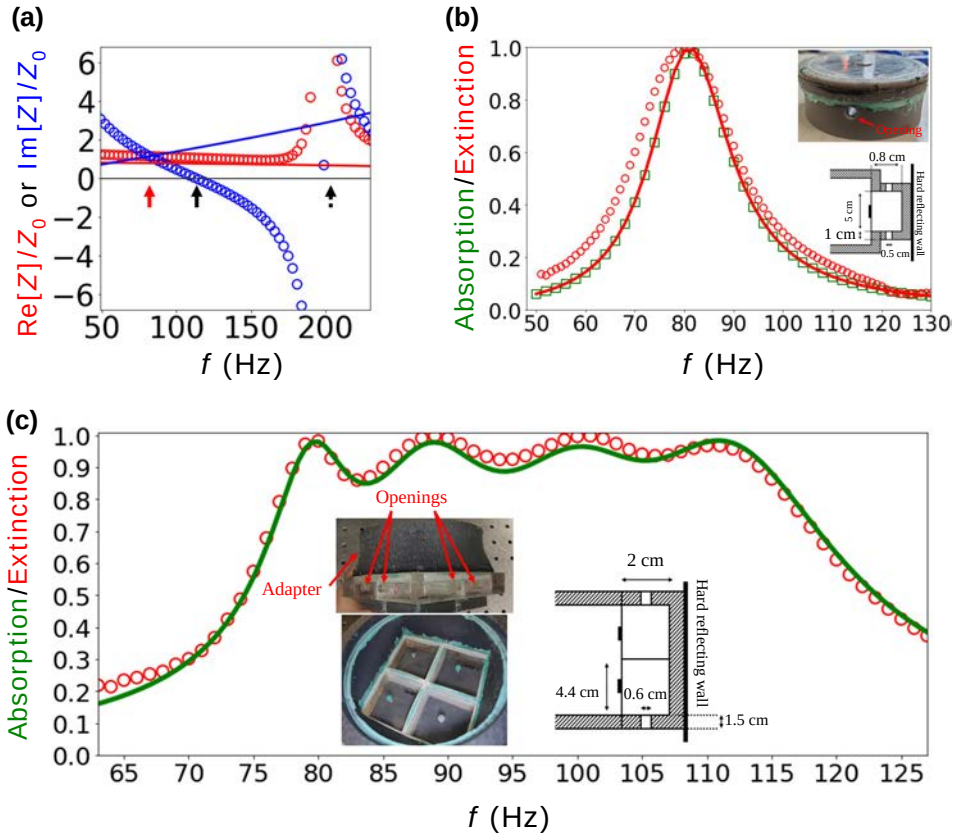

FIG. 4. (a) Red and blue solid lines show the required real and imaginary parts of the decorated-membrane impedance to achieve impedance matching, when it is backed by a cavity with a partial ASBC with three openings on the cavity's sidewall. Red and blue circles, on the other hand, represent the respective real and imaginary parts of the impedance for the decorated membrane alone. Intersection point indicates the frequency at which the impedance-matching condition is satisfied, as designated by the red arrow. Black solid and dashed arrows point to the first resonance and antiresonance frequencies, respectively. (b) Measured absorption spectrum of a decorated-membrane resonator backed by a cavity with three openings. Extinction data obtained from experiments (red circles) and simulation results (red solid line) are plotted as a function of frequency. Absorption from simulations (green squares) are also shown. Coincidence of the extinction and absorption curves implies that the transmission component is very small. Extremely high and broad absorption peak is seen to be centered at 81 Hz. Inset shows a schematic illustration of the hybrid structure, together with a photograph of the sample. (c) Absorption spectrum of four resonators integrated parallel to each other, as shown in the insets. Effective impedance can be expressed as $Z^{-1} = \phi(0.25Z_1^{-1} + 0.25Z_2^{-1} + 0.25Z_3^{-1} + 0.25Z_4^{-1})$, with the absorption $A = 1 - |(Z/Z_0 - 1)/(Z/Z_0 + 1)|^2$. Extinction obtained from experiments (red circles) and absorption obtained from simulations (green solid lines) are shown. Average absorption is 94% in the target range of 80–110 Hz.

While losing the frequency-independent absorption of the ASBC realized by the abrupt cross-section change, here the partial ASBC, when coupled with the DM, involves only the change in the backside-pressure modulation, as introduced by the sidewall openings. This is a much more relaxed condition for applications, especially for confined spaces.

Further broadening of the absorption spectrum can be accomplished by integrating multiple resonators [1,2]. We target 80 to 110 Hz with four resonators, so that the chosen resonance frequencies are $f_1 \approx 80$ Hz, $f_2 \approx 89.0$ Hz, $f_3 \approx 98.8$ Hz, and $f_4 \approx 110.0$ Hz, each with a membrane dimension of 4.4×4.4 cm^2, backed by a 2-cm-deep cavity with two sidewall openings that are 0.6 cm in diameter and 1.5 cm in depth. The four resonators are arranged in parallel to face the sound source, so that their effective surface impedance, Z, and absorption, A, can be expressed as

$$Z^{-1} = \phi\left(\frac{1}{4}Z_1^{-1} + \frac{1}{4}Z_2^{-1} + \frac{1}{4}Z_3^{-1} + \frac{1}{4}Z_4^{-1}\right), \tag{5a}$$

$$A = 1 - \left|\frac{Z/Z_0 - 1}{Z/Z_0 + 1}\right|^2, \tag{5b}$$

where $\phi \approx 91.1\%$ is the area fraction of the membrane. An adapter is used to connect the impedance tube, which has a circular cross section, to the four resonators that have an overall square cross section, as shown in the inset to

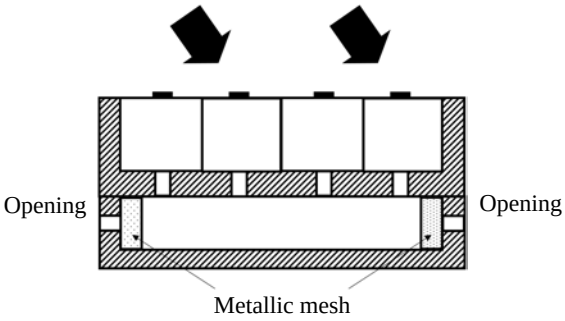

FIG. 5. Schematic diagram of the potential application configuration, where a combination of metallic mesh and openings is placed at the edges of the enclosed backspace to reduce reflection to nearly zero, as described in previous sections.

Fig. 4(c). Red circles and the green solid line represent the measured extinction and simulated absorption spectrum, respectively. The measured absorption in the target frequency range has an average of 94%. As can be seen from Fig. 4(c), this high average absorption is made possible by the broad width of each individual absorption peak, which is the signature of the partial ASBC. If we substitute the measured absorption spectrum into Eq. (1), we obtain $d_{\min} \approx 15.1$ cm, which is 7.5 times our sample thickness.

In actual applications, such a 2×2 structure can be repeatedly placed on a surface, so that it covers a large area. The cavity holes are open to a laterally large but confined space, as shown in Fig. 5. As long as the edges of the backspace have no reflection, the backspace can imitate an infinite space. Such no-reflection conditions can be achieved by utilizing, for example, the combination of a metallic mesh and small openings, as shown in Fig. 5, which we describe in Secs. II and IV.

It should be mentioned that the main difference between the expected performance in applications and the impedance-tube measurement is that the wave can be incident from various directions in actual applications, whereas in impedance measurements the incidence is always normal to the resonators. However, such a difference should have very little effect on the overall performance, as long as the incident angle is not close to 90°. This is because the resonator's lateral dimension is much smaller than the wavelength, so that even at oblique incidence the lateral phase difference on the surface of each resonator is small, implying only a small difference from normal incidence (at which the lateral phase difference is identically zero). However, as the wave's areal energy density also varies with the incident angle, eventually, when the incident angle is close to 90°, the absorption has to approach zero.

VI. CONCLUSION

We present an approach to solve the age-old problem of ultralow-frequency noise absorption, by employing the ASBC or partial ASBC on the absorber's backside. By breaking the implicit assumption of the causality constraint, we show that thin absorbers can provide near-total absorption in the ultralow-frequency range; which was previously considered to be impossible. Our work complements the many approaches that are effective at higher frequencies and delineates a design paradigm for the ultralow-frequency sound absorbers.

ACKNOWLEDGMENTS

P.S. wishes to acknowledge the support of A-HKUST601/18, Research Impact Fund R6015-18, and AoE/P-02/12 for this research.

P.S. conceived the idea and initiated and supervised the research. H.Y.M. designed the sample and the experiment. H.Y.M. and X.Z. carried out simulations. H.Y.M., D.Z., S.M., and T.I. fabricated samples and carried out experiments. P.S. and H.Y.M. wrote the manuscript.

APPENDIX A: EXPERIMENTAL METHODS

The absorption sample is fabricated by sealing layers of metallic meshes in a 3D-printed cylindrical cage. The cage wall is 1.5 − cm -thick solid resin to ensure a negligible amount of leakage around the edge of the sample. The top and bottom faces of the cage are covered by two flat metallic mesh layers with relatively large pore sizes and rigidity, so that they can press the stacked layers into a flat pancake geometry with minimal effect on the surface impedance. Connecting adapters to one side of the cage allows us to mount it at the terminal side of the impedance tube (Brüel & Kjær Type 4206). To extract the effective material parameters of the sample, we sandwich the sample between two segments of the impedance tube. Two sets of microphone slots with 35 and 10 cm separations are used in measurements, so that the measurable frequency can range from 49 to 1540 Hz. Each set of two microphones is connected to two SR830 lock-in amplifiers, such that the absolute pressure amplitude and phase can be detected. The transfer-impedance method suggests that the surface impedance on the front side of a cavity of depth d, filled with an absorber material, is given by [44–46]

$$Z = Z_{\text{eff}} \frac{Z_b - iZ_{\text{eff}} \tan[k_{\text{eff}} d]}{Z_{\text{eff}} - iZ_b \tan[k_{\text{eff}} d]}, \tag{A1}$$

where d is the sample thickness, $Z_{\text{eff}} = \sqrt{\kappa_{\text{eff}} \rho_{\text{eff}}}$ is the material impedance of the absorber, $k_{\text{eff}} = \omega \sqrt{\rho_{\text{eff}} / \kappa_{\text{eff}}}$ is the wavevector, and Z_b is the surface impedance of the cavity's backside boundary. The reflection, r, can be calculated by $r = (Z - Z_0)/(Z + Z_0)$. Equating the calculated real and imaginary part of r to the measured ones yields two equations with four unknowns, namely, the real and imaginary parts of κ_{eff} and ρ_{eff}. Therefore, two measurements with two different Z_b are

carried out to gain sufficient information to find all four unknowns. Here, Z_b can be chosen to have either the value of $Z_{\mathrm{ASBC}} = i0^-$ or $Z_{\mathrm{AHBC}} = i\infty$ in the idealized case, and in actual practice can be easily determined by independent experiments without the absorber. For the metallic mesh that we present in Fig. 2, the effective density and bulk modulus under 500 Hz can be well fitted by $\rho_{\mathrm{eff}} = [214f^{-0.598} + i(8920f^{-0.938})]$ kg/m^3 and $\kappa_{\mathrm{eff}} = [(-127f + 297000) - i(1.30f + 76700)]$ Pa, respectively.

APPENDIX B: SIMULATIONS

Simulations presented in this work are performed by using COMSOL Multiphysics with the "pressure acoustic module" in the frequency domain. To complete a full-waveform simulation, we rebuild the experimental setup model in COMSOL by constructing a sphere with a relatively large radius to imitate the open space in a laboratory. The perfect matching-impedance condition is assigned to the surface of the sphere to ensure that there will be no backscattering. A 5-cm-radius cylinder with a hard-boundary condition is built at the center of the simulation sphere to serve as the impedance tube. By propagating a plane wave along the cylindrical tube, we are able to study the reflection and surface impedance of an unflanged open tube. Figure 6 illustrates a schematic diagram of the model used in the COMSOL simulations. Placing a 20×20 cm^2 hard-boundary D cm away from the opening surface, the gap situation is replicated. The transmission coefficient can be determined by calculating the ratio between the energy flux radiating outward from the tube opening and the input energy. By further assigning κ_{eff} and ρ_{eff} to a section of the circular tube with length t just in front of the open end, both the extinction and absorption coefficients can be easily obtained. The results of these full-waveform simulations are presented in Figs. 1(b) and 3(c) in the main text. However, simulations presented in Figs. 2 and 3(b) are carried out in an easier way, in which Z_{ASBC} is assigned to the termination of the impedance tube. Such simulations sacrifice the consideration of the transmission coefficient and the alteration of the plane-wave form as the sound wave emerges from the open end. Here, the trade-off is a much faster simulation but with somewhat less accuracy. Such simulations are appropriate for those cases where the qualitative trend, rather than the quantitative results, is the focus.

To simulate the performance from the partially open hybrid-membrane resonator, we place the resonator at the end of the waveguide in the setup, while the whole setup is enclosed in a large sphere with an impedance-matching interface as described above. The resonator comprises a decorated membrane covering a shallow cavity with sidewall openings, as shown in the inset of Fig. 4(b). The diameter of both the decorated membrane and the cavity

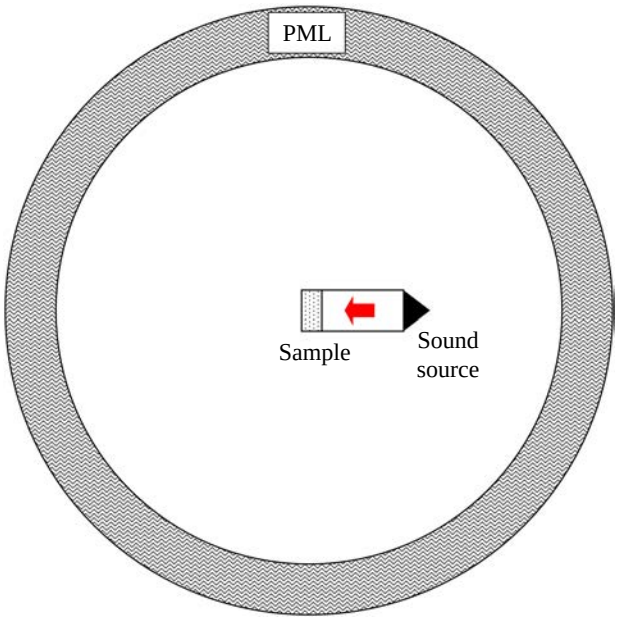

FIG. 6. Schematic diagram of the model used in COMSOL to simulate an open-impedance-tube situation, to capture transmitted sound energy through the opening. At the relevant low-frequency regime, the transmitted sound energy is invariably found to be very small.

is 5 cm, while their thicknesses are 0.2 mm and 0.8 cm, respectively. The mass disk, 1 cm in diameter, is attached to the center of the membrane. The "solid mechanics module" is assigned to the membrane and the mass disk, while the pressure acoustic module is assigned to the cavity. The membrane has a complex initial tension in which the imaginary part serves as the dissipation. It should be noted that, since the diameter of the openings on the cavity sidewall is small, dissipation from the viscous boundary layer from these openings must be considered. This is accounted for by assigning the "narrow region acoustic module" to the openings. The simulated measurements then give us the extinction and absorption curves, as plotted in Fig. 4(b) in the main text.

APPENDIX C: IMPEDANCE-MATCHING CONDITION WITH PARTIAL ASBC

For the case of a decorated membrane backed by a cavity of depth d, we should set $Z_{\mathrm{eff}} = Z_0$ and $k_{\mathrm{eff}} = k$ in Eq. (A1), with an arbitrary boundary condition on the cavity's backside impedance, Z_b. Now, the impedance, as perceived by the incident wave, is given by

$$Z = Z_{\mathrm{DM}} + Z_0 \frac{Z_b - iZ_0 \tan[kd]}{Z_0 - iZ_b \tan[kd]}, \tag{C1}$$

where Z_{DM} denotes the impedance of the decorated-membrane resonator. For impedance matching, it can be

shown that in Eq. (C1) Z_{DM} must have the form $Z_{\mathrm{DM}} = Z_0[1 - i\cot(kd)]$ or $Z_{\mathrm{DM}} = Z_0[1 + i\tan(kd)]$ for $Z_b = i\infty$ (hard boundary) or $Z_b = i0^-$ (soft boundary), respectively [6], so that $Z = Z_0$ from Eq. (C1) as a result. In actual practice, however, the impedance can deviate slightly from Z_0 and still achieve near-total absorption.

In the general case where the impedance contribution from the cavity can be intermediate between the hard and soft Z_b, we can let $Z_b = Z_b^{(r)} + iZ_b^{(i)}$ [$Z_b^{(r)}$ and $Z_b^{(i)}$ being real numbers], and by assuming d to be much smaller than the wavelength, then Z_{DM} must have the form

$$Z_{\mathrm{DM}} = Z_0 \left\{ \left[1 - \frac{Z_b^{(r)} Z_0 (1 + k^2 d^2)}{\Delta} \right] - i \frac{Z_b^{(i)} Z_0 (1 - k^2 d^2) + kd(|Z_b|^2 - Z_0^2)}{\Delta} \right\}, \quad \text{(C2)}$$

in order that $Z = Z_0$, i.e., achieving impedance matching. Here, $\Delta = [Z_0 + Z_b^{(i)} kd]^2 + [Z_b^{(r)} kd]^2$. For a cavity with three holes that open to the outer space, the impedance can be found by using a COMSOL simulation with the narrow region acoustic module assigned to the holes, so that dissipation from the boundary-layer effect is taken into account. Through simulations, it is found that the impedance of the cavity with three openings on the backside of the cavity is almost identical to three openings on the sidewall. Hence, one can use the result with three holes for Z_b, rather than that for the hard wall. It turns out that the Z_b for a plate with three holes can be well fitted by $Z_b = Z_0[(0.00063f + 0.149) - i(0.0126f + 0.075)]$, where f is given in Hz. Substituting this expression for Z_b in Eq. (C2) yields the complex impedance-matching condition as a function of frequency that is plotted as solid lines in Fig. 4(a) in the main text.

While the impedance-matching condition provides a criterion for total absorption, it does not directly tell us the source of dissipation. This can be answered by a COMSOL simulation that provides a more physical picture. The simulation result is illustrated in Fig. 7. We first focus on the air-displacement velocity in the opening region plotted in grayscale, which is normalized to the source-particle velocity defined as $v_0 = P_0/Z_0$, where P_0 is the pressure amplitude of the source. Notice that the darkest regions are inside the holes, this means that the airflow velocity is 2 orders of magnitude higher than that in the other regions. Such an extremely high air-displacement velocity can result in a significant enhancement of the boundary-layer dissipation. On the other hand, the membrane's displacement, normalized to the maximum displacement at its first resonance frequency when the membrane is backed by the PML (perfect matching layer) boundary condition, is also plotted on the colored scale in the same figure. The result indicates that the vibration of the membrane is an order of magnitude larger at the absorption-peak frequency, which also provides dissipation arising from membrane deformation.

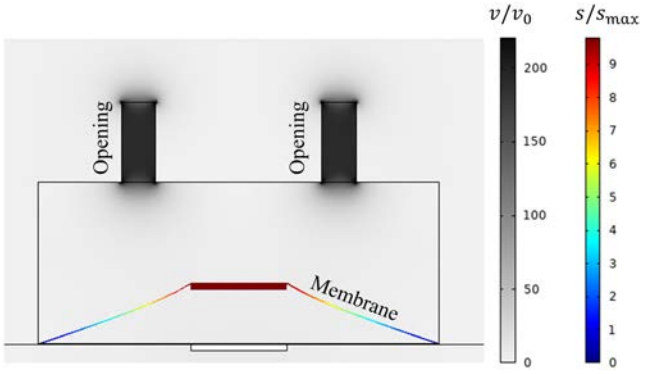

FIG. 7. Airflow velocity and membrane-displacement field at the absorption-peak frequency are plotted in grayscale and colored scale, respectively. Flow velocity is normalized to the source-flow velocity, which is defined as $v_0 = P_0/Z_0$, where P_0 is the wave's amplitude. Membrane displacement, on the other hand, is normalized to the maximum displacement when the membrane is backed by the perfect matching layer boundary condition.

[1] M. Yang and P. Sheng, An integration strategy for acoustic metamaterials to achieve absorption by design, Appl. Sci. **8**, 1247 (2018).

[2] M. Yang, S. Chen, C. Fu, and P. Sheng, Optimal sound-absorbing structures, Mater. Horiz. **4**, 673 (2017).

[3] K. Donda, Y. Zhu, S. Fan, L. Cao, Y. Li, and B. Assouar, Extreme low-frequency ultrathin acoustic absorbing metasurface, Appl. Phys. Lett. **115**, 173506 (2019). A 13 mm thick absorber can achieve near-total absorption at 50 Hz with a fraction of one Hz peak width. It should be noted, however, that the theoretical results shown in Fig. 3 of the publication cannot be compared to the causal limit, owing to the fact that Eq. (8) used for the simulations has overlooked a geometric factor of area fraction (1/9), that should multiply each inverse impedance.

[4] J. Ruan, S. Mosanenzadeh, X. Li, S. Yu, C. Ma, X. Lin, S. Zhang, M. Lu, N. Fang, and Y. Chen, Bimodal hybrid lightweight sound-absorbing material with high stiffness, Appl. Phys. Express **12**, 035002 (2019).

[5] M. Yang and P. Sheng, Sound absorption structures: From porous media to acoustic metamaterials, Ann. Rev. Mat. Res. **47**, 83 (2017).

[6] G. Ma, M. Yang, S. Xiao, Z. Yang, and P. Sheng, Acoustic metasurface with hybrid resonances, Nat. Mater. **13**, 873 (2014).

[7] J. Mei, G. Ma, M. Yang, Z. Yang, W. Wen, and P. Sheng, Dark acoustic metamaterials as super absorbers for low-frequency sound, Nature Commun. **3**, 756 (2012).

[8] X. Zhang, J. Wu, Q. Mao, W. Zhou, and Y. Xiong, Design of a honeycomb-microperforated panel with an adjustable sound absorption frequency, Appl. Acoust. **164**, 107246 (2020).

[9] Y. Liu, H. Zhang, J. Yang, X. Zhang, S. Zhang, L. Fan, and G. Gu, Sound regulation of coupled Helmholtz and Fabry-Pérot resonances in labyrinth cavity structures, Ultrasonics **95**, 45 (2019).

[10] J. Carbajo, S. Ghaffari Mosanenzadeh, S. Kim, and N. Fang, Multi-layer perforated panel absorbers with oblique perforations, Appl. Acoust. **169**, 107496 (2020).

[11] D. Maa, Potential of microperforated panel absorber, J. Acoust. Soc. Am. **104**, 2861 (1998).

[12] C. Shen, Y. Xie, J. Li, S. Cummer, and Y. Jing, Acoustic metacages for sound shielding with steady air flow, J. Appl. Phys. **123**, 124501 (2018).

[13] Z. Tian, C. Shen, J. Li, E. Reit, Y. Gu, H. Fu, S. Cummer, and T. Huang, Programmable acoustic metasurfaces, Adv. Funct. Mater. **30**, 2006376 (2020).

[14] M. Thieury, V. Leroy, J. Dassé, and A. Tourin, Phenomenological law for the acoustic reflection by an array of cylindrical cavities in a soft elastic medium, J. Appl. Phys. **128**, 135106 (2020).

[15] S. Cummer, J. Christensen, and A. Alù, Controlling sound with acoustic metamaterials, Nat. Rev. Mater. **1**, 16001 (2016).

[16] H. Zhang, Z. Wei, X. Zhang, L. Fan, J. Qu, and S. Zhang, Tunable acoustic filters assisted by coupling vibrations of a flexible Helmholtz resonator and a waveguide, Appl. Phys. Lett. **110**, 173506 (2017).

[17] J. Carbajo, S. Ghaffari Mosanenzadeh, S. Kim, and N. Fang, Multi-layer perforated panel absorbers with oblique perforations, Appl. Acoust. **169**, 107496 (2020).

[18] N. Jiménez, V. Romero-García, V. Pagneux, and J. Groby, Rainbow-trapping absorbers: Broadband, perfect and asymmetric sound absorption by subwavelength panels for transmission problems, Sci. Rep. **7**, 13595 (2017).

[19] J. Li and C. Chan, Double-negative acoustic metamaterial, Phys. Rev. E **70**, 055605(R) (2004).

[20] V. Romero-García, N. Jiménez, J. Groby, A. Merkel, V. Tournat, G. Theocharis, O. Richoux, and V. Pagneux, Perfect Absorption in Mirror-Symmetric Acoustic Metascreens, Phys. Rev. Appl. **14**, 054055 (2020).

[21] J. Boulvert, J. Costa-Baptista, T. Cavalieri, V. Romero-García, G. Gabard, E. Fotsing, A. Ross, M. Perna, J. Mardjono, and J. Groby, Folded metaporous material for sub-wavelength and broadband perfect sound absorption, Appl. Phys. Lett. **117**, 251902 (2020).

[22] V. Romero-García, N. Jiménez, G. Theocharis, V. Achilleos, A. Merkel, O. Richoux, V. Tournat, J. Groby, and V. Pagneux, Design of acoustic metamaterials made of helmholtz resonators for perfect absorption by using the complex frequency plane, C. R. Phys. **21**, 713 (2021).

[23] X. Xiang, X. Wu, X. Li, P. Wu, H. He, Q. Mu, S. Wang, Y. Huang, and W. Wen, Ultra-open ventilated metamaterial absorbers for sound-silencing applications in environment with free air flows, Extreme Mech. Lett. **39**, 100786 (2020).

[24] J. Groby, R. Pommier, and Y. Aurégan, Use of slow sound to design perfect and broadband passive sound absorbing materials, J. Acoust. Soc. Am. **139**, 1660 (2016).

[25] C. Lagarrigue, J. Groby, V. Tournat, O. Dazel, and O. Umnova, Absorption of sound by porous layers with embedded periodic arrays of resonant inclusions, J. Acoust. Soc. Am. **134**, 4670 (2013).

[26] M. Yang, C. Meng, C. Fu, Y. Li, Z. Yang, and P. Sheng, Subwavelength total acoustic absorption with degenerate resonators, Appl. Phys. Lett. **107**, 104104 (2015).

[27] N. Zheludev and Y. Kivshar, From metamaterials to metadevices, Nat. Mater. **11**, 917 (2012).

[28] Y. Liu and X. Zhang, Metamaterials: A new frontier of science and technology, Chem. Soc. Rev. **40**, 2494 (2011).

[29] Y. Duan, J. Luo, G. Wang, Z. Hang, B. Hou, J. Li, P. Sheng, and Y. Lai, Theoretical requirements for broadband perfect absorption of acoustic waves by ultra-thin elastic meta-films, Sci. Rep. **5**, 12139 (2015).

[30] G. Liu, Y. Zhou, M. Liu, Y. Yuan, X. Zou, and J. Cheng, Acoustic waveguide with virtual soft boundary based on metamaterials, Sci. Rep. **10**, 981 (2020).

[31] D. Blackstock, *Fundamentals of Physical Acoustics* (Wiley, New York, 2000), pp. 112–290.

[32] Y. Ra'di, C. Simovski, and S. Tretyakov, Thin Perfect Absorbers for Electromagnetic Waves: Theory, Design, and Realizations, Phys. Rev. Appl. **3**, 037001 (2015).

[33] C. Fu, X. Zhang, M. Yang, S. Xiao, and Z. Yang, Hybrid membrane resonators for multiple frequency asymmetric absorption and reflection in large waveguide, Appl. Phys. Lett. **110**, 021901 (2017).

[34] T. Cox and P. D'Antonio, *Acoustic Absorbers and Diffusers*, 3rd ed. (CRC Press, Boca Raton, 2016), pp. 91–130.

[35] F. Han, G. Seiffert, Y. Zhao, and B. Gibbs, Acoustic absorption behaviour of an open-celled aluminium foam, J. Phys. D **36**, 294 (2003).

[36] G. Theocharis, O. Richoux, V. García, A. Merkel, and V. Tournat, Limits of slow sound propagation and transparency in lossy, locally resonant periodic structures, New J. Phys. **16**, 093017 (2014).

[37] J. P. Dalmont, J. Kergomard, and X. Meynial, Realization of an anechoic termination for sound ducts at low-frequencies, C. R. Acad. Sci. Paris **309**, 453 (1989).

[38] Z. Kang and Z. Ji, Acoustic length correction of duct extension into a cylindrical chamber, J. Sound Vib. **310**, 782 (2008).

[39] J. Mercier, J. Marigo, and A. Maurel, Influence of the neck shape for helmholtz resonators, J. Acoust. Soc. Am. **142**, 3703 (2017).

[40] M. Atig, J. Dalmont, and J. Gilbert, Termination impedance of open-ended cylindrical tubes at high sound pressure level, C. R. Mec. **332**, 299 (2004).

[41] H. Levine and J. Schwinger, On the radiation of sound from an unflanged circular pipe, Phys. Rev. **73**, 383 (1948).

[42] V. Leroy, N. Chastrette, M. Thieury, O. Lombard, and A. Tourin, Acoustics of bubble arrays: Role played by the dipole response of bubbles, Fluids **3**, 95 (2018).

[43] M. Yang, G. Ma, Y. Wu, Z. Yang, and P. Sheng, Homogenization scheme for acoustic metamaterials, Phys. Rev. B **89**, 064309 (2014).

[44] W. Thomson, Transmission of elastic waves through a stratified solid medium, J. Appl. Phys. **21**, 89 (1950).

[45] H. Utsuno, T. Tanaka, T. Fujikawa, and A. Seybert, Transfer function method for measuring characteristic impedance and propagation constant of porous material, J. Acoust. Soc. Am. **85**, S77 (1989).

[46] N. Jiménez, V. Romero-García, and J. Groby, Perfect absorption of sound by rigidly-backed high-porous materials, Acta Acust. Acust. **104**, 396 (2018).